Subcycle interference dynamics of time-resolved photoelectron holography with midinfrared laser pulses

Xue-Bin Bian,[1,*] Y. Huismans,[2] O. Smirnova,[3] Kai-Jun Yuan,[1] M. J. J. Vrakking,[2,3,†] and André D. Bandrauk[1,‡]

[1]*Département de Chimie, Université de Sherbrooke, Sherbrooke, Québec J1K 2R1, Canada*

[2]*FOM Institute AMOLF, Science Park 113, NL-1098 XG Amsterdam, The Netherlands*

[3]*Max-Born-Institut, Max Born Straße 2A, D-12489 Berlin, Germany*

Time-resolved photoelectron holography from atoms using midinfrared laser pulses is investigated by solving the corresponding time-dependent Schrödinger equation (TDSE) and a classical model, respectively. The numerical simulation of the photoelectron angular distribution of Xe irradiated with a low-frequency free-electron laser source agrees well with the experimental results. Different types of subcycle interferometric structures are predicted by the classical model. Furthermore with the TDSE model it is demonstrated that the holographic pattern is sensitive to the shape of the atomic orbitals. This is a step toward imaging by means of photoelectron holography.

PACS number(s): 32.80.Wr, 33.60.+q, 61.05.jp, 31.15.A−

I. INTRODUCTION

The study of electronic dynamics with long-wavelength (low-frequency) laser pulses has received increasing attention recently due to the possibility of controlling ionized electrons at high intensities, including control of laser-induced recollision [1–3]. Some unexpected features have been observed, such as a characteristic spike-like structure at low energy in the photoelectron energy distribution [4,5] and a giant resonance from inner-shell electrons of Xe in HHG [6]. It has also been shown that a photoelectron holography [7,8] pattern that contains extensive time-resolved information can be clearly recorded with midinfrared laser fields. As illustrated in Fig. 1, the photoelectron holography pattern comes from the interference between scattered and unscattered electron trajectories [9]. The holography encodes temporal and spatial information about both the core and the recollision electrons [7]. It is a subcycle interference phenomenon [7,8,10–12] due to the subcycle time scale of recollision event [1,2]. The unscattered electrons can be viewed as a reference, which encodes the information of the initial state, whereas the scattered electrons can be seen as a signal, which contains the information of the scattering core. For short-wavelength laser fields, this holography pattern may be less clear due to the influence of the core on the reference wave. Huismans *et al.* [7] have recently recorded clear holographic pictures by using a midinfrared free-electron laser (FEL) source. When the electron is tunnel ionized by the low-frequency laser field [1], it will appear at some distance from the core. Thus the influence of the core on the reference wave will be greatly reduced. In this paper, we explore the dynamics of photoelectron holography by investigating the *above-threshold ionization* (ATI) of Xe and H atoms in midinfrared laser pulses numerically. A simulation that is based on solving the corresponding time-dependent Schrödinger equation (TDSE) agrees well with the experimental results. The subcycle

dynamics of interference in ATI is further studied by a classical model which reproduces the observed interference patterns well. In addition, the possible observation of several subcycle interference patterns is predicted. Furthermore, based on comparing TDSE calculations for different initial orbitals, we conclude that photoelectron holography can give information on atomic orbitals [13].

The paper is organized as follows. We briefly introduce the numerical method for solving the TDSE in Sec. II; the classical model to investigate the subcycle dynamics is presented in Sec. III. The state-dependent holography of H is shown in Sec. IV. The conclusion is given in Sec. V.

II. HOLOGRAPHY BY FULL QUANTUM SIMULATIONS

A. Theoretical method for TDSE

For numerically solving the TDSE, it was shown previously that the velocity gauge is the preferred gauge, as it greatly reduces the total angular momentum number L_{max} compared to the length gauge [14]. Thus we solve the TDSE in the velocity gauge [atomic units (a.u.) $e = m = \hbar = 1$ are used throughout unless otherwise stated],

$$i\frac{\partial}{\partial t}\Psi(\mathbf{r},t) = \left[\frac{1}{2}\mathbf{p}^2 + V_e(\mathbf{r}) - \mathbf{A}(t)\cdot\mathbf{p}\right]\Psi(\mathbf{r},t). \quad (1)$$

For the H atom, the potential $V_e(r) = -1/r$. For Xe, we use the form of an effective model potential $V_e(r)$ [15,16] in the single-active-electron approximation (SAEA) to describe both the atomic structure of the bare atom and the rescattering properties of the ion core:

$$V_e(r) = -(1 + a_1 e^{-a_2 r} + a_3 r e^{-a_4 r} + a_5 e^{-a_6 r})/r, \quad (2)$$

with $a_1 = 51.356$, $a_2 = 2.112$, $a_3 = -99.927$, $a_4 = 3.737$, $a_5 = 1.644$, and $a_6 = 0.431$. Spin-orbit coupling is neglected. The calculated ionization potential energies I_p from the ground state $5p$ and the first excited state $6s$ are 12.1 and 3.9 eV, respectively, and agree well with the ionization energies of $5p[^1S]_{J=0}$ (12.1 eV) and $6s[^2P_{3/2}]_{J=2}$ (3.8 eV) [17]. The validity of the SAEA has been discussed in Ref. [15]. It works

* xb.bian@usherbrooke.ca

† marc.vrakking@mbi-berlin.de

‡ andre.bandrauk@usherbrooke.ca
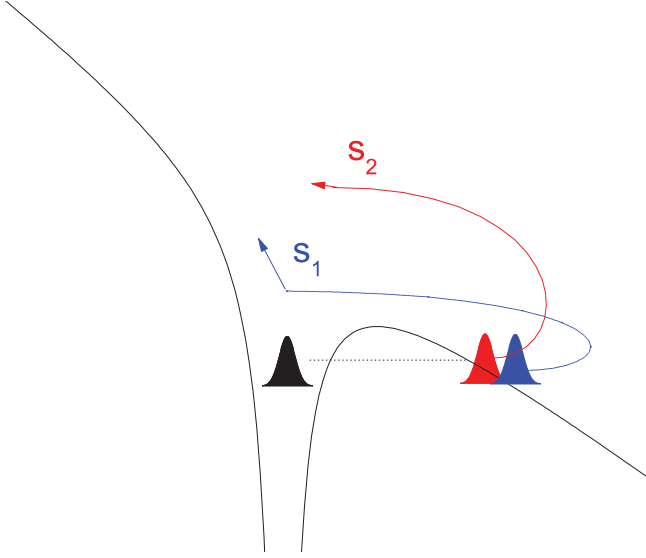
FIG. 1. (Color online) Schematic illustration of interference trajectories in photoelectron holography. Trajectory S_1: after tunnel ionization, the electron is accelerated in the laser field, then driven back and scattered by the core. Trajectory S_2: the ionized electron oscillates in the laser field without being scattered.

well in tunneling ionization. In addition, the initial state of Xe in this work is the first excited state $6s$. Because of the lower ionization potential of the $6s$ state compared to that of the $5p$ outer shell state, the SAEA model in the low-frequency laser field is a quite good approximation.

We use a cosine square function to represent the temporal profile of the laser pulse. Assuming that the polarization of the laser field is along the z axis, the field vector potential reads

$$\mathbf{A}(t) = \frac{E_0}{\omega} \cos^2 \left(\frac{\pi t}{\tau} \right) \sin(\omega t + \delta) \mathbf{e}_z, \quad (3)$$

where τ is the total duration of the pulse, ω is the angular frequency, E_0 is the amplitude, and δ is the carrier-envelope phase (CEP). The resulting electric field $E(t) = -\frac{\partial \mathbf{A}}{\partial t}$ satisfies the total zero area $\int E(t) dt = 0$.

For accurate calculation of the ATI, direct TDSE simulation is still a challenging problem. The kinetic energy of a scattered electron can be as high as $10 U_p$, where U_p is known as the ponderomotive energy $U_p = E_0^2 / 4\omega^2$. In midinfrared laser pulses, U_p (which scales with λ^2) can reach appreciable values. In addition, the total time duration $\tau \propto \lambda$ and high angular momenta l must be included. An ATI spectrum converged up to $10 U_p$ requires a radius $r_{max} = 0.55\tau\sqrt{2 \times 10 U_p}$ [18]. As a result, for the same number of laser cycles and laser intensities, the computation demand for an 8-μm laser field is at least 100 times larger than for an 800-nm laser field. Thus it is important to choose a flexible basis expansion in the radial direction, rather than equally distributed grid points to accurately represent the electronic wave function in intense midinfrared laser fields. As described in Refs. [18,19], a B-spline basis is a localized basis, resulting in a sparse Hamiltonian matrix, which greatly reduces the required memory on the computer. In addition, a B-spline basis is efficient to describe the continuum states [18]. Thus we expand the time-dependent wave function

by a radial basis of B splines and an angular basis of spherical harmonics as:

$$\Psi(\mathbf{r}, t) = \sum_{l=0}^{L_{max}} \sum_{i=1}^{N} C_i^l(t) \frac{B_i^k(r)}{r} Y_l^0(\theta, \phi), \quad (4)$$

where N is the number of B splines for each angular momentum l, k is the order of the B-spline basis, and $C_i^l(t)$ are time-dependent coefficients. For a linearly polarized laser field, the magnetic quantum number is conserved, which is set $m_l = 0$ in this paper. Inserting Eq. (4) in Eq. (1) leads to

$$i\mathbf{S}\frac{\partial \mathbf{C}}{\partial t} = \mathbf{H}\mathbf{C}, \quad (5)$$

where $\mathbf{C}$ is a vector of coefficients with dimension $N_{max} = (L_{max} + 1)N$, and $\mathbf{S}$ and $\mathbf{H}$ are the overlap and Hamiltonian matrices, respectively. Due to the localized B-spline basis and the orthonormality of spherical harmonics, the matrices $\mathbf{S}$ and $\mathbf{H}$ are block-banded matrices; the corresponding expressions can be found in Refs. [20,21].

For the propagation of the time-dependent wave function $\Psi(\mathbf{r}, t)$, we use the Arnoldi-Lanczos scheme [22,23]. Defining $\mathbf{H}' = \mathbf{S}^{-1}\mathbf{H}$, the essential idea of the Arnoldi-Lanczos method is to construct the Krylov space of $\mathbf{H}'$,

$$\mathcal{K}_m(\mathbf{H}', \mathbf{C}) = \text{span}\{\mathbf{C}, \mathbf{H}'\mathbf{C}, \dots, (\mathbf{H}')^{(m-1)}\mathbf{C}\}, \quad (6)$$

which is generated by the Lanczos iteration. The procedure yields a matrix $\mathbf{V}$ with dimension $N_{max} \times m$, which transforms matrix $\mathbf{H}'$ into a tridiagonal symmetric matrix $\mathbf{h}$ with a small-order m. The time-dependent coefficients $\mathbf{C}(t + \Delta t)$ are obtained by the relation

$$\mathbf{C}(t + \Delta t) = \mathbf{V} \exp(-i \Delta t \mathbf{h}) \mathbf{V}^\dagger \mathbf{C}(t). \quad (7)$$

The ATI spectrum $P(E)$ can be extracted from the total time-dependent wave function $\Psi(\mathbf{r}, t)$, Eq. (4), at the end of the pulse by projection on the discretized continuum wave function $\Phi_{E_k}^l(r)$ obtained by diagonalization of the field-free Hamiltonian,

$$\frac{dP(E)}{dE} = \sum_{l=0}^{L_{max}} \left| \left\langle \Phi_{E_k}^l(\mathbf{r}) \middle| \Psi(\mathbf{r}, \tau) \right\rangle \right|^2, \quad (8)$$

where $\Phi_{E_k}^l(\mathbf{r})$ is normalized on the energy scale [18].

To calculate the photoelectron angular distribution (PAD), we compute the differential spectrum:

$$\frac{\partial P(E_k, \theta_k)}{\partial E_k \partial \theta_k} = |\langle \psi_{\mathbf{k}}^-(\mathbf{r}) | \Psi(\mathbf{r}, \tau) \rangle|^2, \quad (9)$$

where the Coulomb continuum wave function $\psi_{\mathbf{k}}^-(\mathbf{r})$ is expanded in terms of spherical harmonics:

$$\psi_{\mathbf{k}}^-(\mathbf{r}) = \sum_{l=0}^{L_{max}} (i)^l \exp^{-i\eta_l} \Phi_{E_k}^l(\mathbf{r}) Y_l^0(\theta_k, 0), \quad (10)$$

where η_l is the Coulombic phase.

B. Comparison of the theoretical and experimental photonelectron momentum distribution of Xe

For the solution of the TDSE, Eq. (1), we use the parameters: $\lambda = 7$ μm and a 10-cycle time duration τ to match
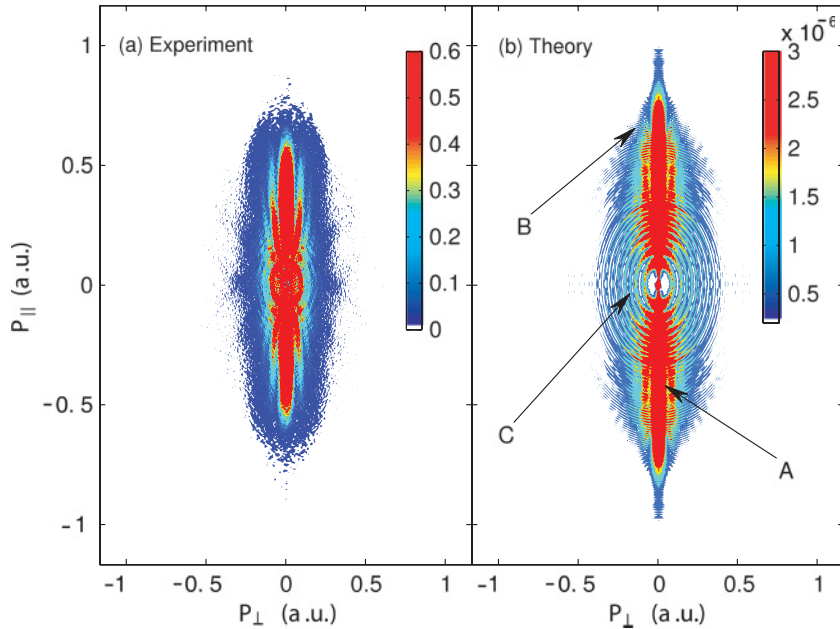
FIG. 2. (Color online) Comparison of experimental (a) and theoretical (b) photoelectron momentum distribution of Xe. The initial state is the metastable 6s state, the laser intensity is $I = 7.1 \times 10^{11}$ W/cm^2, and the wavelength is 7 μm.

the experimental FEL parameters in Ref. [7]. It is expected that CEP effects can be neglected for long multicycle pulses, thus we set $\delta = 0$. The maximum total angular momentum number is $L_{max} = 39$, the number of B splines for each partial wave is $N = 5000$, and the box of the radial direction is confined to $r_{max} = 4500$ a.u. The integration time step is $\Delta t = 0.048$ a.u., and the dimension of the reduced Krylov space is $m = 16$.

In Ref. [7], Huismans *et al.* measured 3D photoelectron velocity map images experimentally at different laser intensities. The initial state was the metastable 6s state and was prepared by means of electron impact. Figure 2(a) shows a slice through the experimental 3D photoelectron momentum distribution for a peak laser intensity $I = 7.1 \times 10^{11}$ W/cm^2. For comparison, our theoretical result is presented in Fig. 2(b), showing satisfactory agreement between theoretical and experimental results. From the theoretical result, we can clearly identify three different kinds of interference patterns in the momentum distribution spectrum. As illustrated in Fig. 2(b), the interference pattern A resembles a "fork." It can be clearly identified in both theoretical simulation and experimental measurement. The interference pattern B is a set of semirings centered on a point in momentum space around momentum $P_\parallel = \pm 0.7$ a.u. It is weak and therefore not possible to identify in the experimental results. The pattern C is merely a set of outgoing rings from the center around $P = 0$ a.u., which can be well resolved in both Figs. 2(a) and 2(b). It is the familiar ATI structure, corresponding to the absorption of photons in excess of the minimum number needed to reach the ionization threshold.

In Ref. [7], the observed interference patterns were interpreted by using a number of theoretical approaches, which included numerical solution of the TDSE for an Ar atom, a Coulomb-corrected SFA treatment (where the influence of the Coulomb field on the signal and reference trajectories was considered), and a semianalytical treatment that rationalized the holographic interferences in terms of the geometrical difference between the signal and reference trajectories and the interaction of the electrons with the laser electric field.

Since the simulations by TDSE for Ar in Ref. [7] and Xe in the present paper agree well with the experimental results, the holography is not very dependent on the atomic target. To further rationalize interference patterns A–C, discussed above, in what follows we use a simple classical model [1,2,24] to identify the subcycle interference dynamics.

III. HOLOGRAPHY BY A CLASSICAL MODEL

The analysis of holographic structures in angular resolved ATI spectra based on application of the saddle-point approach to the standard S-matrix expressions in the strong-field approximation has been performed in Ref. [7] (see Supplementary on-line material). Here we consider a simplified picture based on the classical recollision three-step model [1,2]. It is based on the following assumptions [1,2].

(i) The free electron is born at distance $z_0 = I_p/E_0$ from the core by tunneling ionization. After ionization, we neglect the influence of the Coulomb potential due to the large z_0 and α (where $\alpha = E_0/\omega^2$ is the maximum excursion of a free electron in the laser field) for the current laser parameters. When the electron comes back to the core, it is elastically scattered.

(ii) The initial velocity of the scattered electron is $v_\parallel^{signal} = v_\perp^{signal} = 0$ (i.e., between ionization and recollision the signal trajectory is along the polarization axis), while the initial velocity of the unscattered electron is $v_\parallel^{ref} = 0, v_\perp^{ref} \neq 0$ (i.e., the reference electron acquires its transverse velocity during the ionization process). Due to the long excursion time between ionization and recollision, if $v_\perp^{signal} \neq 0$, the electron will not return to the core [1].

(iii) After scattering, the velocity of the signal electron is the same as that of the reference electron. This is a condition for the observation of the interference pattern.

(iv) We neglect the phase changes during the tunnel ionization and the scattering process. We further neglect multiple scattering of the signal electron by the core.

Since the laser field is polarized along the z direction, the motion of the electrons along the perpendicular direction is conserved in the laser field. In the following, we only consider the motion of electrons along the z direction. If the electron is ionized at a particular phase φ of the electric field $E(t) = E_0 \cos(\omega t + \varphi)$, the velocity and the position of the electron can be obtained as

$$v(t,\varphi) = \int_0^t -E(t')dt' = -\frac{E_0}{\omega}[\sin(\omega t + \varphi) - \sin(\varphi)], \quad (11)$$

$$z(t,\varphi) = \int_0^t v(t')dt'$$
$$= \frac{E_0}{\omega^2}[\cos(\omega t + \varphi) - \cos(\varphi) + \omega \sin(\varphi)t] - z_0. \quad (12)$$

When the electron is driven back to the core after traveling time t_c, $z(t_c,\varphi) = 0$, and we have a relation between t_c and φ as

$$\cos(\omega t_c + \varphi) - \cos(\varphi) + \omega \sin(\varphi)t_c = \gamma^2/2, \quad (13)$$

where $\gamma = \sqrt{2I_p}\omega/E_0$ is the Keldysh parameter.

Next we assume that the signal electron is elastically scattered by the core at an angle θ_c. After that, the velocity in the perpendicular direction is constant as $v_\perp = v(t_c,\varphi) \sin(\theta_c)$. The final velocity along the z direction is

$$v_\parallel(t) = \int_{t_c}^t E(t')dt'$$
$$= -\frac{E_0}{\omega}[\sin(\omega t) - \sin(\omega t_c)] + v(t_c,\varphi)\cos(\theta_c). \quad (14)$$

Here we take into account that the vector potential $A(t) = 0$ after the end of the pulse. Thus, the momentum measured at the detector is

$$P_\parallel = \frac{E_0}{\omega}\sin(\omega t_c) + v(t_c,\varphi)\cos(\theta_c). \quad (15)$$

The phase accumulated between the reference (with ionization phase φ') and the scattered signal waves does not change after the recollision of the signal electron. Therefore, the time t^r up to which the phase accumulation of the
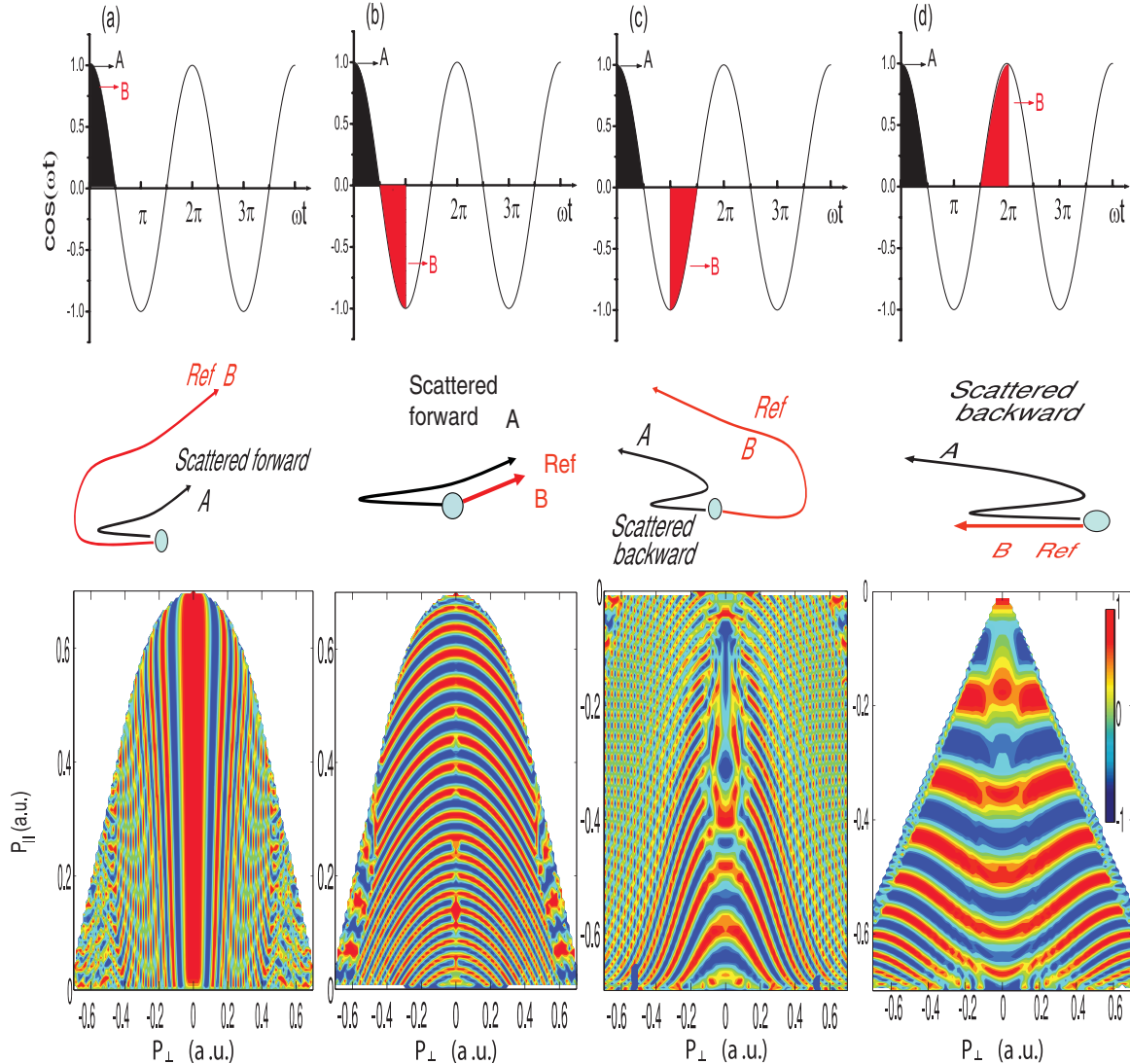
FIG. 3. (Color online) Sketch of different subcycle interference trajectories and the corresponding interferometric structures. The laser parameters are the same as in Fig. 2. In the upper panel, A stands for the signal electron, B represents the reference electron.

reference wave packet needs to be calculated is the time interval between the collision time of the signal wave packet and the ionization time for the reference wave packet. Thus in our notation, $\varphi + \omega t_c = \varphi' + \omega t^r$ (t_c is calculated from the ionization time of the signal wave, t^r is calculated from the given formula). In addition, $v_{\parallel}^r(t^r, \varphi') = v(t_c, \varphi) \cos(\theta_c)$, $v_{\perp}^r = v(t_c, \varphi) \sin(\theta_c)$.

From the above discussion, we can get the phase difference between the reference electron and the signal electron as

$$\Delta \Phi = \int_0^{t_c} \frac{v^2(t', \varphi)}{2} dt' - \int_0^{t^r} \frac{v^2(t', \varphi')}{2} dt' - \frac{v_{\perp}^2 t^r}{2} - I_p \frac{(\varphi - \varphi')}{\omega}. \tag{16}$$

We discuss next the subcycle interference dynamics. As shown in Fig. 3, we fix the ionization of the signal electron in the first quarter-cycle with $\varphi \in [0, \pi/2]$. This electron is first ionized in the negative z direction and is then turned around by the laser field, so that the velocity of the signal electron arriving at the core is positive before being scattered. Next we consider the interference patterns that are generated by the interference of this signal electron in combination with a reference electron that is ejected during the same quarter-cycle or one of the first three-quarter cycles after this one. Though it may not be possible to separate all these interference patterns experimentally, separate evaluation of different interfering contributions to the overall spectrum is useful, since it provides insight into the experimental results and in the TDSE calculations.

We first consider the case where the reference electron is generated in the same quarter-cycle $\varphi' \in [0, \pi/2]$. The interference pattern for this case is presented in Fig. 3(a) and agrees well with the pattern shown in Fig. 2(b), labeled A. If the reference electron is generated in the next quarter-cycle with $\varphi' \in [\pi/2, \pi]$, the interference pattern is shown in Fig. 3(b). This is a ring pattern centered at $P = 0$ a.u. The velocity of the reference electron generated with $\varphi' \in [0, \pi]$ is positive when the signal electron arrives at the core, which implies that the interference patterns in Figs. 3(a) and 3(b) correspond to forward scattering interference. Although somewhat similar in appearance, the interference pattern in Fig. 3(b) is not the usual ATI pattern C spaced by one photon energy in Fig. 2(b), which is produced by multiple-cycle laser pulses. Nor does it correspond to the time double-slit interference reported by Gopal *et al.* [10], which corresponds to the interference between two non-rescattering reference electrons, rather than the interference between a rescattering signal electron and a non-rescattering reference electron. A calculation of the time double-slit interference trajectories and the corresponding interferometric structures within the framework of the classical model is presented in Fig. 4. This interference is particularly easy to understand; it arises from the interference of two wave packets ionized at instants t_1 and t_2 within the same laser cycle, for which $A(t_1) = A(t_2)$, where the laser electric field has opposite values, $E(t_1) = -E(t_2)$. That is, the two wave packets appear on the opposite sides of the ion but have the same drift momentum. In other words, the signal electron goes across the core without being rescattered. It is interesting to note that the holographic interference pattern shown in Fig. 3(b) is a set of
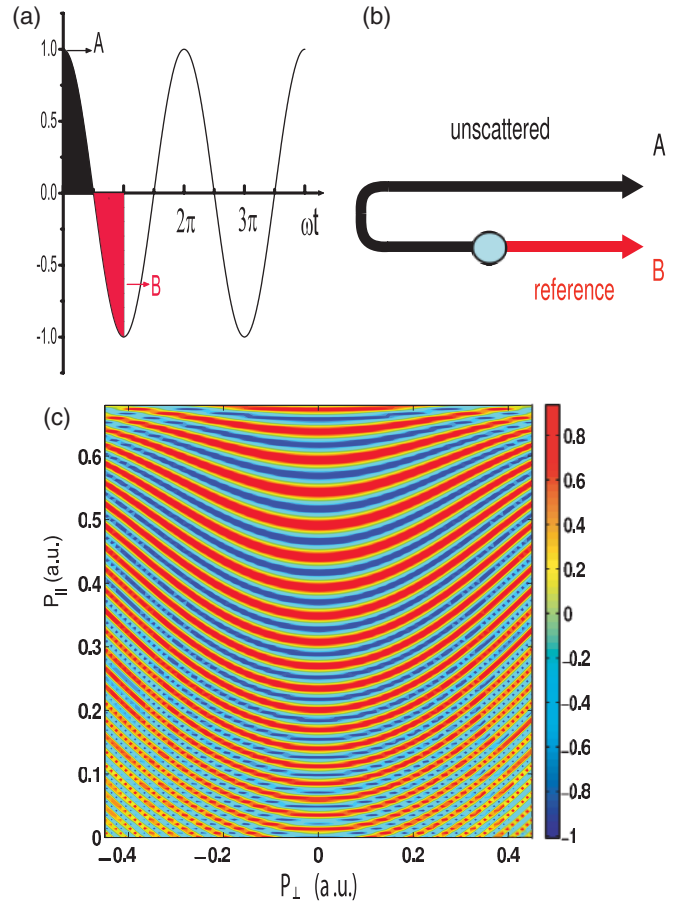
FIG. 4. (Color online) Sketch of time double-slit interference trajectories and the corresponding interferometric structures by the classical model. Laser parameters are the same as in Fig. 2. A stands for the signal electron; B represents the reference electron.

outgoing rings (i.e., rings with an upward curvature), while the time double-slit interference pattern presented in Fig. 4(c) is a set of incoming rings (downward curvature).

So far we have considered the subcycle interference pattern in forward scattering. Now we turn to the holographic structures that appear in backward scattering. If the reference electron is generated in the third quarter-cycle with $\varphi' \in [\pi, 3\pi/2]$, the interference pattern shown in Fig. 3(c) is obtained. This pattern is a semiring structure centered around $P_{\parallel} = -0.7$ a.u., which agrees with the pattern labeled B in Fig. 2(b). However, we cannot definitely say that pattern B in Fig. 2(b) is caused by the interference in Fig. 3(c) since the time double-slit interference pattern illustrated in Fig. 4(c) has a somewhat similar structure [7,10–12].

If the reference electron is ionized in the fourth quarter-cycle with $\varphi' \in [3\pi/2, 2\pi]$, the interference structure is presented in Fig. 3(d). It is difficult to resolve these structures in the experimental and theoretical spectra in Fig. 2. In the results shown in Figs. 3(c) and 3(d), the reference electron has a negative velocity, whereas the signal electron arrives at the core with a positive velocity. Therefore the results in both Figs. 3(c) and 3(d) involve backward scattering of the signal wave, which usually is weaker than the forward scattering. This is the reason why the interference patterns in Figs. 3(c)
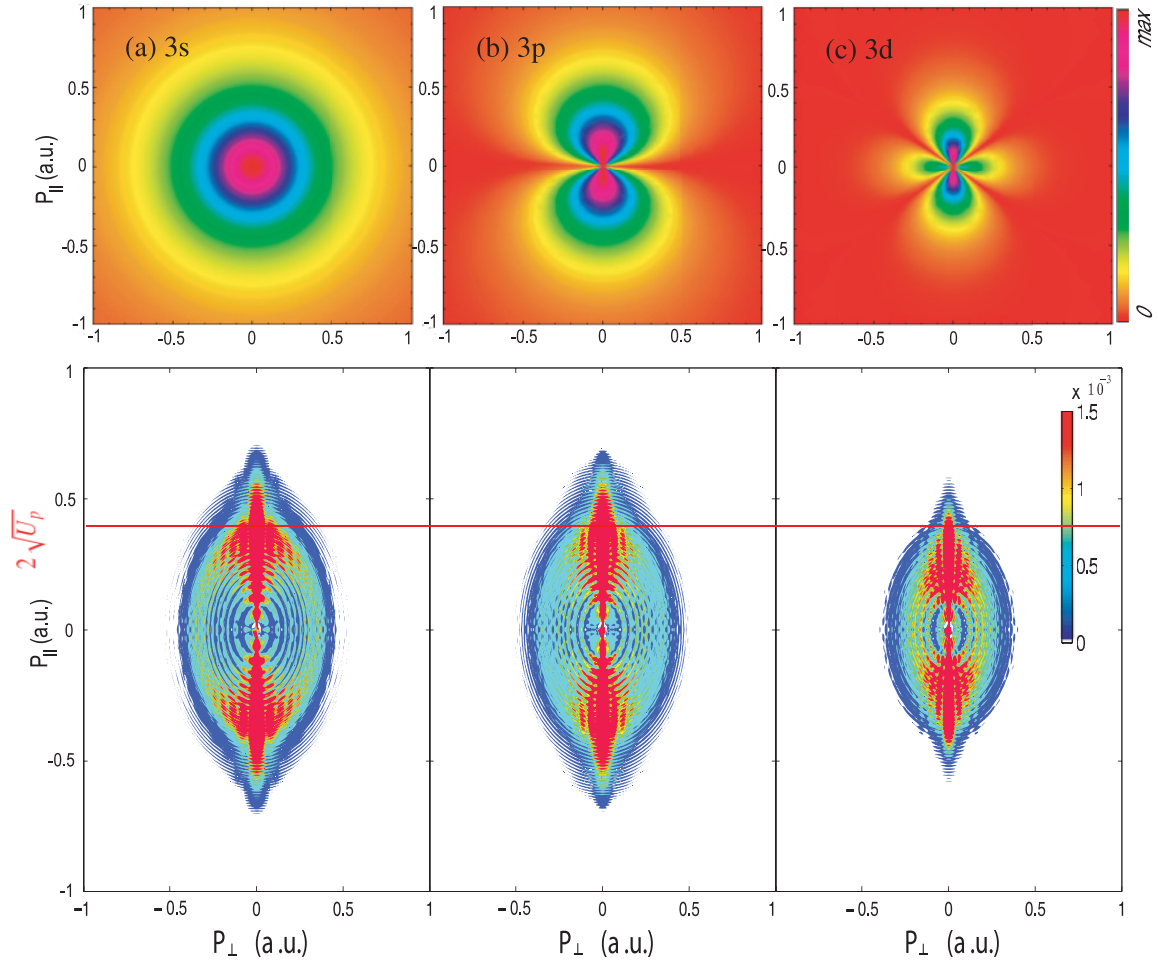
FIG. 5. (Color online) Atomic orbitals of H in momentum space and the corresponding photoelectron momentum distribution in a laser field with intensity $I = 1.775 \times 10^{11}$ W/cm^2 and wavelength 7 μm. The initial state is (a) $3s$, (b) $3p$, and (c) $3d$. The horizontal (red) line corresponds to the cutoff momentum of the directly ionized electrons.

and 3(d) are difficult to be identified in the experimental results in Fig. 2(a).

IV. IMPRINT OF DEGENERATE ORBITALS OF THE H ATOM IN HOLOGRAPHY

Photoelectron holographic patterns contain both time and spatial information [7]. In this light it would be interesting to investigate the possibility of resolving the shape of the atomic orbital with photoelectron holography. As described in the previous section, there are four types of holographic interference structures, which should all carry valuable information. Realistically, however, only the interference structure described in Fig. 3(a) will be resolvable, since it is the only interference pattern in the angular direction. All other interference patterns, including the nonholographic ones, have a pattern in the radial direction and will be hard to disentangle. From now on we therefore focus on the first interference structure and explore to what extent these interference patterns depend on the choice of initial orbital.

To reduce the influence of the tunneling time and the ionization rate of the different initial states, we choose the degenerate $3s$, $3p$, and $3d$ states of H as initial states. The photoelectron

momentum distributions, calculated with the TDSE, are presented in Fig. 5. Different initial orbitals indeed give rise to different holographic patterns and three types of differences can be observed; the width of the pattern, the cutoff of the pattern, and the shape of the fringes. Concerning the first, for both the $3s$ and the $3d$ state, multiple fringes can be observed, while for the $3p$ state the second fringe is already barely visible. This can be explained by the initial distribution of the photoelectrons; the more the photoelectrons initially ionize with an orthogonal component $P_\perp$, the wider the final pattern. The perpendicular momentum distribution of the unscattered photoelectrons is closely related to the initial state $\Psi(0)$ [25,26]:

$$\Psi(P_\perp) = \Psi(0) \exp\left[-\frac{P_\perp^2 \tau_0}{2} \right], \qquad (17)$$

where $\tau_0 = \sqrt{2I_p}/E_0$ in the static limit. The shapes of the atomic orbitals in momentum space are presented in the top panel in Fig. 5. Both the s and the d state have a substantial distribution in the orthogonal direction, while for the $3p$ state there is a nodal plane perpendicular to the z axis with $P_\parallel = 0$ a.u. Consequently, the reference photoelectrons ionized in

the perpendicular direction are suppressed, giving rise to a narrower distribution of the holographic pattern.

The second observation is the lower momentum cutoff in the interference pattern for the $3d$ orbital compared to the $3s$ and $3p$ orbitals. The cutoff energy of the directly ionized electron is $2U_p$, which restricts the holographic pattern below $2\sqrt{U_p}$ in momentum space. Photoelectrons with a higher energy, up to $10U_p$, can also be obtained by backscattering [24]. A possible explanation for the lower cutoff of $3d$ orbitals could be related to the effective potential $\frac{l(l+1)}{2r^2} - \frac{1}{r}$, which is strongly dependent on l. A high angular momentum changes the shape of the tunneling wave packet and the tunneling rate [27]. The ionization rate of electrons from $3d$ orbitals with higher energy decreases compared to that of electrons from $3s$ and $3p$ orbitals. The momentum distribution of electrons from the $3s$ and $3p$ states extends beyond $2\sqrt{U_p}$, which corresponds to a stronger recollision signal. However, the recollision is suppressed for the $3d$ state due to the centrifugal potential (preventing the return).

The third, and perhaps most important, observation is the shape of the fringes itself. While for $3s$ they are parallel to the main lobe, for $3p$ they bend together at higher momenta and for $3d$ they diverge. A possible explanation is the different short-range potentials altering the phase of the scattering wave packets in a different way for the three atomic orbitals. This would imply that it is possible to map the atomic orbital [13,28] with photoelectron holography.

The observation and analysis so far are qualitative, but the TDSE calculations do show that the atomic orbitals have an imprint on the final pattern. It would be very interesting to investigate the possibility of time-resolving atomic orbitals with photoelectron holography.

V. CONCLUSION

In summary, we present and compare accurate numerical methods to calculate ATI spectra of atoms in midinfrared laser pulses. The simulations agree well with current experimental results performed with a FEL source. A simple classical model is proposed to interpret the subcycle interference patterns obtained. To our knowledge, the subcycle interference patterns shown in Figs. 3(b)–3(d) have not been reported previously. We have demonstrated that all subcycle interferences give a pattern in the radial direction except for the holographic pattern created by electron wave packets generated in the same quarter-cycle. This allows us to disentangle this holographic pattern from other interference structures and investigate the time and spatial information stored in the hologram. TDSE calculations show that this holographic pattern is sensitive to the degenerate $3s$, $3p$, and $3d$ states of the H atom, which implies that the shape of the original orbital is imprinted in the photoelectron hologram. This opens the way to investigation of the possibility of doing time-resolved studies of atomic and molecular orbitals with photoelectron holography. Further research may benefit from sculpturing and tailoring these new pulses using control algorithms [29].

[1] P. B. Corkum, Phys. Rev. Lett. **71**, 1994 (1993).

[2] A. D. Bandrauk, S. Chelkowski, and S. Goudreau, J. Mod. Opt. **52**, 411 (2005).

[3] T. M. Yan, S. V. Popruzhenko, M. J. J. Vrakking, and D. Bauer, Phys. Rev. Lett. **105**, 253002 (2010).

[4] C. I. Blaga, F. Catoire, P. Colosimo, G. G. Paulus, H. G. Muller, P. Agostini, and L. F. DiMauro, Nature Phys. **5**, 335 (2009).

[5] W. Quan *et al.*, Phys. Rev. Lett. **103**, 093001 (2009).

[6] A. D. Shiner, B. E. Schmidt, C. Trallero-Herrero, H. J. Wörner, S. Patchkovskii, P. B. Corkum, J-C. Kieffer, F. Légaré, and D. M. Villeneuve, Nature Phys. **7**, 464 (2011).

[7] Y. Huismans *et al.*, Science **331**, 61 (2011).

[8] M. Spanner, O. Smirnova, P. B. Corkum, and M. Y. Ivanov, J. Phys. B **37**, L243 (2004).

[9] G. G. Paulus, F. Grasbon, A. Dreischuh, H. Walther, R. Kopold, and W. Becker, Phys. Rev. Lett. **84**, 3791 (2000).

[10] R. Gopal *et al.*, Phys. Rev. Lett. **103**, 053001 (2009).

[11] D. G. Arbó, E. Persson, and J. Burgdörfer, Phys. Rev. A **74**, 063407 (2006).

[12] F. Lindner, M. G. Schätzel, H. Walther, A. Baltuška, E. Goulielmakis, F. Krausz, D. B. Milošević, D. Bauer, W. Becker, and G. G. Paulus, Phys. Rev. Lett. **95**, 040401 (2005).

[13] J. Itatani, J. Levesque, D. Zeidler, H. Niikura, H. Pépin, J. C. Kieffer, P. B. Corkum, and D. M. Villeneuve, Nature **432**, 867 (2004).

[14] E. Cormier and P. Lambropoulos, J. Phys. B **30**, 77 (1997).

[15] X. M. Tong and C. D. Lin, J. Phys. B **38**, 2593 (2005).

[16] D. B. Milošević, W. Becker, M. Okunishi, G. Prümper, K. Shimada, and K. Ueda, J. Phys. B **43**, 015401 (2010).

[17] [http://www.nist.gov/index.html].

[18] H. Bachau, E. Cormier, P. Decleva, J. E. Hansen, and F. Martín, Rep. Prog. Phys. **64**, 1815 (2001).

[19] X. B. Bian and A. D. Bandrauk, Phys. Rev. A **83**, 023414 (2011).

[20] L. Y. Peng and A. F. Starace, J. Chem. Phys. **125**, 154311 (2006).

[21] Y. C. Han and L. B. Madsen, Phys. Rev. A **81**, 063430 (2010).

[22] T. J. Park and J. C. Light, J. Chem. Phys. **85**, 5870 (1986).

[23] X. X. Guan, O. Zatsarinny, K. Bartschat, B. I. Schneider, J. Feist, and C. J. Noble, Phys. Rev. A **76**, 053411 (2007).

[24] G. G. Paulus, W. Becker, W. Nicklich, and H. Walther, J. Phys. B **27**, L703 (1994).

[25] N. B. Delone and V. P. Krainov, J. Opt. Soc. Am. B **8**, 1207 (1991).

[26] M. Y. Ivanov, M. Spanner, and O. Smirnova, J. Mod. Opt. **52**, 165 (2005).

[27] A. M. Perelomov, V. S. Popov, and M. V. Terent'ev, Zh. Eksp. Teor. Fiz. **50**, 1393 (1966) [Sov. Phys. JETP **23**, 924 (1966)].

[28] T. Zuo, A. D. Bandrauk, and P. B. Corkum, Chem. Phys. Lett. **259**, 313 (1996).

[29] A. B. Yedder, C. Le Bris, O. Atabek, S. Chelkowski, and A. D. Bandrauk, Phys. Rev. A **69**, 041802(R) (2004).